



RESEARCH LETTER

10.1029/2021GL096244

Special Section:

Modeling in glaciology

On the Limitations of Using Polarimetric Radar Sounding to Infer the Crystal Orientation Fabric of Ice Masses

Nicholas M. Rathmann¹ , David A. Lilien^{1,2} , Aslak Grinsted¹, Tamara A. Gerber¹ , Tun Jan Young³ , and Dorthe Dahl-Jensen^{1,2}

¹Niels Bohr Institute, University of Copenhagen, Copenhagen, Denmark, ²Centre for Earth Observation Science, University of Manitoba, Winnipeg, MB, Canada, ³Scott Polar Research Institute, University of Cambridge, Cambridge, UK

Key Points:

- Radar returns over glacier ice are, for normal incidence, insensitive to whether or not a vertical principal fabric direction exists
- The harmonic mode responsible for a nonvertical principal fabric direction might be determined from oblique radar sounding
- Assuming a vertical principal fabric direction when there is none can substantially affect inferred directional viscosities of glacier ice

Supporting Information:

Supporting Information may be found in the online version of this article.

Correspondence to:

N. M. Rathmann,
rathmann@nbi.ku.dk

Citation:

Rathmann, N. M., Lilien, D. A., Grinsted, A., Gerber, T. A., Young, T. J., & Dahl-Jensen, D. (2022). On the limitations of using polarimetric radar sounding to infer the crystal orientation fabric of ice masses. *Geophysical Research Letters*, 49, e2021GL096244. <https://doi.org/10.1029/2021GL096244>

Received 4 OCT 2021

Accepted 8 DEC 2021

© 2021. The Authors.

This is an open access article under the terms of the [Creative Commons Attribution License](https://creativecommons.org/licenses/by/4.0/), which permits use, distribution and reproduction in any medium, provided the original work is properly cited.

Abstract We introduce a transfer matrix model for radio-wave propagation through layered anisotropic ice that permits an arbitrary dielectric permittivity tensor in each layer. The model is used to investigate how crystal orientation fabrics without a vertical principal direction affect polarimetric radar returns over glaciers and ice sheets. By expanding the *c*-axis orientation distribution in terms of a spherical harmonic series, we find that radar returns from synthetic fabric profiles are relatively insensitive to the harmonic mode responsible for a nonvertical principal direction; however, only for normally incident waves. Consequently, the strength of this mode might be relatively difficult to infer in glaciers and ice sheets, which in turn has implications for the ability to determine the full second-order structure tensor, needed to infer the local flow regime, flow history, or to represent the directional viscosity structure of glacier ice for ice-flow modeling.

Plain Language Summary The orientation of ice crystals in glacier ice locally co-evolve with and can enhance the flow of ice. Methods that allow inferring the crystal structure inside glaciers and ice sheets are, therefore, essential for improving the accuracy and realism of ice-flow models, and have broad implications for understanding past and present flow regimes. In this work, we introduce a new radio-wave model and use it to investigate the extent to which radar surveys over glaciers and ice sheets can reveal the orientation information necessary to improve such ice-flow models and construct a proxy for past flow. We show that conventional polarimetric radar surveys, which look straight down, might be poorly suited for the task; a specific but important component of the grain orientation structure cannot be seen with such surveys. We find, however, that radio waves transmitted at an angle to the surface might overcome this crucial limitation and allow the full crystal structure to be inferred.

1. Introduction

Single crystals of ice and olivine are both viscously (Bai et al., 1991; Duval et al., 1983) and elastically (Gammon et al., 1983; Kumazawa & Anderson, 1969) anisotropic. Thus, as the crystal orientation fabric (henceforth *fabric*) evolves during flow in polycrystalline glacier ice or in the mineral aggregate of the upper mantle, so should the bulk directional viscosity and elasticity structure. Being able to infer fabrics in situ is central for validating large-scale anisotropic ice-flow models and geodynamical models of mantle flow processes; models that might lead to a better understanding of, for example, streaming ice (Lilien et al., 2021) and the coupling between plate motions and the sublithospheric mantle (e.g., W. Wang & Becker, 2019), respectively. Furthermore, fabric anisotropy provides a unique constraint on the past and present deformation in the lithosphere and sublithospheric mantle (Fouch & Rondey, 2006). Likewise, in the limit of weak dynamic recrystallization, ice fabrics might provide a proxy for past and present flow regimes (Thorsteinsson et al., 2003; Wilson & Peternell, 2011) that could reveal the existence of paleo ice streams (Lilien et al., 2021; Llorens et al., 2021).

Measuring seismic shear-wave splitting (seismic birefringence caused by elastic anisotropy) is recognized as an important approach for determining the in situ fabrics of glacier ice (Diez & Eisen, 2015; Hellmann et al., 2021; Kerch et al., 2018) and the upper-mantle (Long & Becker, 2010 and references therein). Glacier ice is, in addition, also optically birefringent over radio frequencies (Hargreaves, 1978). Radio-echo sounding surveys provide, therefore, another way to infer the fabrics of glaciers and ice sheets: for carefully constructed surveys, radio-echo return signals (radar returns) contain information about the bulk dielectric permittivity with depth, which in turn depends on the second-order structure tensor, $\langle \mathbf{c} \otimes \mathbf{c} \rangle$, of the local grain *c*-axis distribution, $\psi(\theta, \phi)$ (Figure 1a) (elaborated on below). In a sense, $\langle \mathbf{c} \otimes \mathbf{c} \rangle$ measures the coarsest degree of fabric anisotropy by characterizing the

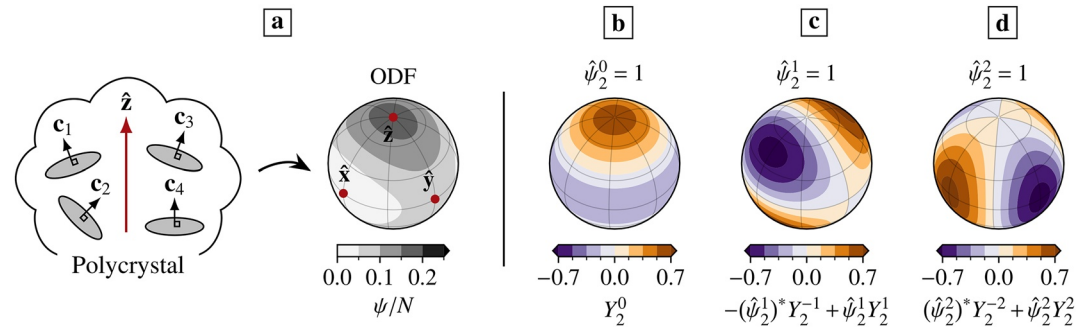


Figure 1. The c -axis orientation distribution function (ψ/N) of a polycrystal (a), and the lowest-order harmonic modes that $\langle \mathbf{c} \otimes \mathbf{c} \rangle$, and therefore $\langle \epsilon_g \rangle$, depends on (b–d). The harmonic modes may be arbitrarily scaled and rotated around $\hat{\mathbf{z}}$ depending on the real and imaginary parts of the expansion coefficients $\hat{\psi}_2^m$, here shown for values of 1.

average outer product of c -axis orientations (lowest-order nonvanishing moment of ψ). Coincidentally, $\langle \mathbf{c} \otimes \mathbf{c} \rangle$ is also a central quantity needed for anisotropic ice-flow modeling (e.g., Gillet-Chaulet et al., 2005) and for constructing the elasticity tensor of a polycrystal (see Supporting Information S1).

Modeling radio-wave propagation has recently received renewed interest as an important tool for supporting the interpretations of radar surveys. Recent examples include among others Jordan et al. (2020) who estimated the prevailing horizontal c -axis direction and magnitude of the horizontal fabric asymmetry within the Whillans Ice Stream, Young, Schroeder, et al. (2021) who quantified and revealed large-scale trends in fabric asymmetry and orientation over the Eastern shear margin of Thwaites Glacier, and Ershadi et al. (2021) who proposed a minimization problem for inferring the eigenvalues of $\langle \mathbf{c} \otimes \mathbf{c} \rangle$ with depth at the EDC and EDML ice-core sites in Antarctica.

Few anisotropic radio-wave propagation models have generally been developed for glaciological applications (e.g., Dall, 2020; Fujita et al., 2006; Wang & Wong, 2020; Wang et al., 2009; Warren et al., 2016), and a common limiting model constraint is that $\langle \mathbf{c} \otimes \mathbf{c} \rangle$ must have a vertical principal direction (elaborated on below), with only a few exceptions (Matsuoka et al., 2009). While arguably relevant in many places throughout ice sheets, this constraint restricts the extent to which modeling can aid interpretations of radar returns over areas where the fabric profile is poorly known. Put differently, the error made by assuming a vertical principal direction, when in fact there is none, is not well understood. Fabrics with double clusters of c -axes have, for example, been observed in shear-dominated regimes where discontinuous dynamic recrystallization is active, both in deformation tests (Bouchez & Duval, 1982; Qi et al., 2019) and in natural settings (Jackson & Kamb, 1997; Monz et al., 2021). For vertical shear with active discontinuous dynamic recrystallization, the otherwise vertical principal direction (center of orientation mass) may hence be displaced toward the horizontal plane. As another example, Lilien et al. (2021) recently modeled the strain-induced rotation of c -axes inside an idealized ice stream, finding that fabrics may tilt at least 8° under a combination of extensional flow and vertical shear. Such tilt angles have also been suggested to exist below or near ice divides (Martín et al., 2009).

In this article, we introduce a general transfer matrix model for radio-wave propagation through layered anisotropic ice that permits an arbitrary dielectric permittivity tensor, and hence arbitrary orientation fabric, in each layer. Our model therefore overcomes the fundamental assumption often made in previously developed models, namely that the orientation fabric has a vertically aligned eigenbasis ($\langle \mathbf{c} \otimes \mathbf{c} \rangle$ has a vertical principal direction). Using the new model, we quantify the error made by assuming $\langle \mathbf{c} \otimes \mathbf{c} \rangle$ has a vertical principal direction (when in fact it does not) by modeling radar returns from synthetic fabric profiles, and discuss the implications for experimentally inferring the fabrics of ice masses. Finally, we end by briefly discussing how our methodology might be adapted for elastic (seismic) plane-wave propagation.

Vectors and tensors are denoted by boldface lower- and upper-case symbols, respectively, for example, \mathbf{a} and \mathbf{B} , with the exception of the electric field, \mathbf{E} . Matrix multiplication is written as $\mathbf{B}\mathbf{a} = B_{ij}a_j$, the dot product as $\mathbf{a} \cdot \mathbf{b} = a_i b_i$, and the outer product as $\mathbf{a} \otimes \mathbf{b} = a_i b_j$, where repeated indices are summed over. The complex conjugate is denoted by superscript “*”, and the matrix transpose by superscript “T”.

2. Permittivity of a Polycrystal

The complex dielectric permittivity of a single ice crystal, ϵ_g , is uniaxial (Fujita et al., 2000):

$$\epsilon_g = \begin{bmatrix} \epsilon_{\perp} & 0 & 0 \\ 0 & \epsilon_{\perp} & 0 \\ 0 & 0 & \epsilon_{\parallel} \end{bmatrix}, \quad (1)$$

where $\epsilon_{\parallel} = \epsilon'_{\parallel} - i\epsilon''_{\parallel}$ and $\epsilon_{\perp} = \epsilon'_{\perp} - i\epsilon''_{\perp}$ are the principal relative permittivities parallel and perpendicular to the optical c -axis, and $\epsilon'_{\perp}, \epsilon'_{\parallel}$ and $\epsilon''_{\perp}, \epsilon''_{\parallel}$ are the real and imaginary parts, respectively. For wavelengths much longer than the average grain size, the bulk permittivity of a polycrystal is, effectively, the grain-ensemble-averaged permittivity (Hargreaves, 1978, see Supporting Information S1)

$$\langle \epsilon_g \rangle = \frac{2\epsilon_{\perp} + \epsilon_{\parallel}}{3} \mathbf{I} + (\epsilon_{\parallel} - \epsilon_{\perp}) \left(\langle \mathbf{c} \otimes \mathbf{c} \rangle - \frac{1}{3} \mathbf{I} \right), \quad (2)$$

where impurities are disregarded for now. The first contribution in Equation 2 is an isotropic (monopole) contribution, equal to the average permittivity of a single grain. The second contribution is a quadrupole contribution that depends on the lowest-order structure tensor characterizing the fabric anisotropy, $\langle \mathbf{c} \otimes \mathbf{c} \rangle$. The quadrupole contribution vanishes if either the single-grain permittivity is isotropic ($\epsilon_{\perp} = \epsilon_{\parallel}$; not the case for ice), or if the fabric is isotropic to lowest order ($\langle \mathbf{c} \otimes \mathbf{c} \rangle = \mathbf{I}/3$). Note that Equation 2 is exact.

Suppose we expand the c -axis distribution, ψ , in terms of a spherical harmonic series:

$$\psi(\theta, \phi) = \sum_{l=0}^L \sum_{m=-l}^l \psi_l^m Y_l^m(\theta, \phi), \quad (3)$$

where ψ_l^m are the complex expansion coefficients, and L is the wave-mode truncation above which finer-scale structure in ψ is unresolved. In this case, the total number of grains is simply $N = \sqrt{4\pi}\psi_0^0$, and ψ being real implies that $\psi_l^{-m} = (-1)^m (\psi_l^m)^*$. The orientation distribution function (ODF) is by definition the normalized c -axis distribution ψ/N and depends therefore on the normalized modes $\hat{\psi}_l^m = \psi_l^m / \psi_0^0$.

Given the expansion (Equation 3), the entries of $\langle \mathbf{c} \otimes \mathbf{c} \rangle$ depend linearly on $\hat{\psi}_2^m$ (Rathmann et al., 2021; see also Supporting Information S1). That is, two complex numbers ($\hat{\psi}_2^1, \hat{\psi}_2^2$) and a real number ($\hat{\psi}_2^0$) are sufficient to determine $\langle \mathbf{c} \otimes \mathbf{c} \rangle$, and therefore $\langle \epsilon_g \rangle$, exactly. The magnitudes (absolute values) of the three coefficients $\hat{\psi}_2^0, \hat{\psi}_2^1$, and $\hat{\psi}_2^2$, determine how strongly the harmonic modes shown in Figures 1b–1d contribute to the ODF, respectively, while the complex phases of $\hat{\psi}_2^1$ and $\hat{\psi}_2^2$ determine how the contributions from the two horizontally anisotropic modes (Figures 1c and 1d) are rotated around the $\hat{\mathbf{z}}$ axis. The advantage of the spectral basis is therefore made clear: the effect of a nonvertical principal direction on $\langle \epsilon_g \rangle$ is dictated solely by the magnitude and phase of $\hat{\psi}_2^1$ (Figure 1c).

3. Transfer Matrix Model

We consider the problem of electromagnetic plane-wave propagation through a multi-layered anisotropic medium by adapting the 4×4 transfer matrix formalism from the optics community (Passler et al., 2020; Passler & Paarmann, 2017; Xu et al., 2000; Yeh, 1980), as recently suggested by Wang and Wong (2020) who also considered glaciological applications but assumed normal incidence and a fabric with a vertical principal direction. A couple of important differences between the optical and radioglaciological application of this method should be emphasized: (a) optical applications typically involve a continuously illuminated multi-layered medium (for which the method's solution is exact), whereas radar systems used in glaciology emit transient pulses, and (b) in radioglaciological applications the electromagnetic energy budget is not strictly closed in the sense that repeated reflections of internal interfaces are neglected, as well as absorption and reflection at the ice-bed interface.

In addition to using a spectral-space representation of fabric for calculating $\langle \epsilon_g \rangle$, what makes this work novel is, therefore, the adaption of the 4×4 formalism to radioglaciology, which involves re-casting the 4×4 problem of

a continuously illuminated multi-layered medium into a 2×2 form relevant for polarized incident pulses. In the following, we briefly elaborate by introducing the background for the 4×4 formalism. For readers less interested in technical details, it is possible to skip to the subsection “Radar returns” where the corresponding 2×2 transfer matrix model is introduced in analogy to the celebrated model by Fujita et al. (2006).

3.1. Background

The permittivity tensor of a given layer is diagonal if $\langle \mathbf{c} \otimes \mathbf{c} \rangle$ is isotropic or has a vertical principal direction and is rotated into its horizontal eigenbasis. In either case, normally incident plane-wave propagation reduces to a decoupled problem in the independent p and s modes (electric field polarization parallel and perpendicular to the plane of incidence, respectively). As a consequence, multi-layered models typically involve the manipulation of 2×2 matrices (e.g., Fujita et al., 2006). In the general case of obliquely incident waves in birefringent media with nonzero off-diagonal elements in the permittivity tensor, the total radiation consists of four partial plane waves, and mode coupling takes place at interfaces (Yeh, 1980). Layered models that allow for arbitrary dielectric tensors, and hence arbitrary orientation fabrics, therefore involve the manipulation of 4×4 matrices.

To elaborate, consider a plane wave propagating in the $\hat{\mathbf{x}}\text{-}\hat{\mathbf{z}}$ plane of a semi-infinite isotropic medium with wave vector \mathbf{k}_0 , where $\hat{\mathbf{z}}$ is positive in the upwards direction. Let the wave be incident on an anisotropic layer below that is horizontally homogeneous and has a permittivity of $\epsilon_0\epsilon$ and a scalar permeability of $\mu_0\mu$. Here, ϵ_0 and μ_0 are the permittivity and permeability in vacuum, respectively, and ϵ and μ are the relative values. Given the plane of incidence, we follow Passler and Paarmann (2017) by writing:

$$\mathbf{k}_0 = \frac{\omega}{c} [\xi, 0, q_0]^\top, \quad (4)$$

where ω is the angular frequency of the wave, $c = 1/\sqrt{\mu_0\epsilon_0}$, and ξ and q_0 are the dimensionless x - and z -components of the wave vector, respectively. The x -component is related to the angle of incidence, α , by $\xi = \sqrt{\epsilon_{\text{inc}}}\sin(\alpha)$, where ϵ_{inc} is the relative isotropic dielectric constant of the incident medium (Xu et al., 2000). Due to horizontal homogeneity, the x and y wave-vector components of the transmitted and reflected waves are conserved. The wave vectors permitted in the anisotropic medium, \mathbf{k}_1 , therefore have ξ in common with the incident medium, implying $\mathbf{k}_1 = \omega/c[\xi, 0, q_1]^\top$. The z -component, q_1 , is meanwhile constrained by the wave equation in momentum space (based on Maxwell's equations) for the electric field \mathbf{E} :

$$\mathbf{k}_1 \times (\mathbf{k}_1 \times \mathbf{E}) + \left(\frac{\omega}{c}\right)^2 \mu \epsilon \mathbf{E} = \mathbf{0}. \quad (5)$$

Written in component form, the wave equation is:

$$\begin{bmatrix} \mu\epsilon_{xx} - q_1^2 & \mu\epsilon_{xy} & \mu\epsilon_{xz} + \xi q_1 \\ \mu\epsilon_{yx} & \mu\epsilon_{yy} - \xi^2 - q_1^2 & \mu\epsilon_{yz} \\ \mu\epsilon_{zx} + \xi q_1 & \mu\epsilon_{zy} & \mu\epsilon_{zz} - \xi^2 \end{bmatrix} \begin{bmatrix} E_x \\ E_y \\ E_z \end{bmatrix} = \mathbf{0}, \quad (6)$$

for which nontrivial solutions require the determinant of the matrix to vanish, yielding a quartic equation in q_1 with four roots. Let therefore:

$$\mathbf{k}_{1j} = \frac{\omega}{c} [\xi, 0, q_{1j}]^\top \quad (7)$$

denote the four wave-vector solutions ($j = 1, 2, 3, 4$) of the anisotropic layer. The four solutions consist of two forward (downward) propagating modes and two reverse (upward) propagating modes (Yeh, 1980), here sorted such that indices $j = 1, 2$ and $j = 3, 4$ refer to the downward and upward propagating modes, respectively. We furthermore sort the solutions into p -polarized ($j = 1, 3$) and s -polarized ($j = 2, 4$) modes, or, in the case of birefringent media, ordinary wave modes ($j = 1, 3$) and extraordinary wave modes ($j = 2, 4$). The sorting convention follows Passler et al. (2020) and Passler and Paarmann (2017).

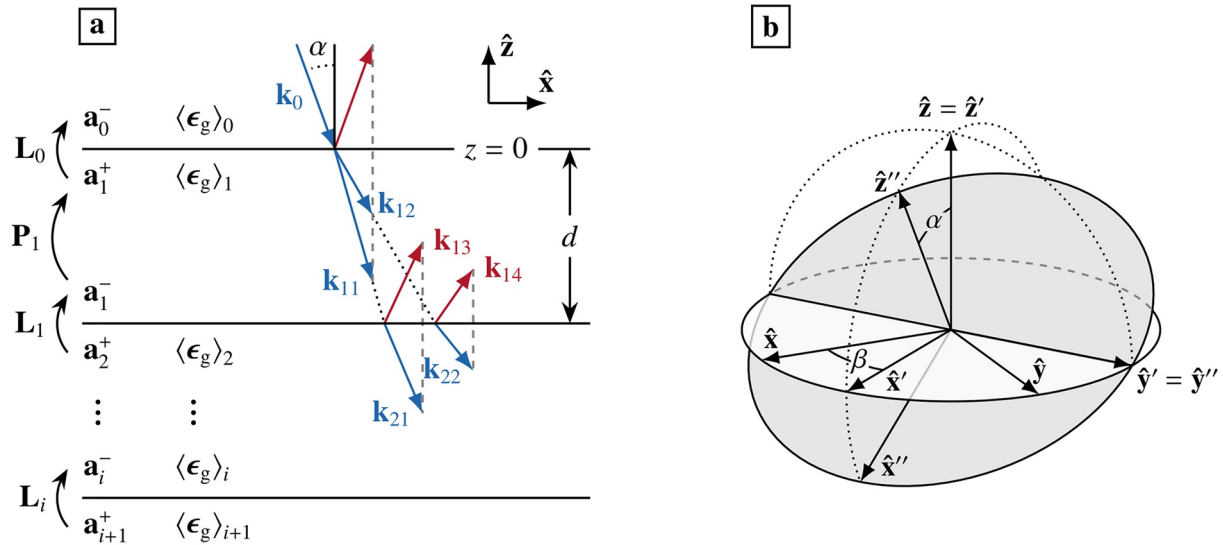


Figure 2. (a): Transfer matrix formalism that allows the four partial-wave amplitudes to be calculated throughout the layer stack by matrix multiplication of the interface (\mathbf{L}_i) and propagation (\mathbf{P}_i) matrices with the partial-wave amplitude vector (\mathbf{a}_i). The plane wave is incident in layer $i = 0$ with angle of incidence α . Each layer is assumed to be horizontally homogeneous and characterized by an anisotropic, complex permittivity tensor, $\langle \epsilon_g \rangle_i$, which depends on the second-order structure tensor of the layer, $(\mathbf{c} \otimes \mathbf{c})_i$. (b): Fabric ($\hat{x}, \hat{y}, \hat{z}$) and measurement ($\hat{x}'', \hat{y}'', \hat{z}''$) coordinate systems. The angle β represents a rotation in the horizontal plane about \hat{z} , while the angle of incidence, α , represents a rotation about \hat{y}' . The antennae “H” and “V” directions are parallel to \hat{x}'' and \hat{y}'' , respectively, defining the measurement coordinate system (gray plane). The plane of incidence is the \hat{x}'' – \hat{z}'' plane.

Inserting the solutions Equation 7 into Equation 6 and solving for \mathbf{E} , the (normalized) eigenpolarizations can be calculated for $j = 1, 2, 3, 4$ (not shown for brevity, see Xu et al., 2000 for analytical expressions), and the total electric field in the anisotropic layer is the sum of the four partial plane waves (see Supporting Information S1). At this point, however, the partial-wave complex amplitudes are unconstrained because the wave equation is homogeneous; that is, the partial-wave amplitudes are the model unknowns to be sought after.

3.2. Multilayered Medium

We are interested in the four partial plane-wave amplitudes as a function of depth in a multi-layered medium, composed of vertically stacked horizontally homogeneous layers of equal thickness, d , but with different permittivity tensors. Let the subscript i denote the layer number for layer-wise quantities, ranging from $i = 0$ in the incident layer and increasing with depth (Figure 2a). The bulk permittivity of the i th layer, $\langle \epsilon_g \rangle_i$, is taken to be Equation 2. Here, we follow Fujita et al. (2006) by neglecting all but the primary internal interface reflections, even if the spacing between internal interfaces is comparable to the radar wavelength. Note that internal interfaces are assumed perfectly straight such that microscopic scattering caused by interface roughness can be neglected.

Let

$$\mathbf{a}_i^\pm = [a_{i1}^\pm, a_{i2}^\pm, a_{i3}^\pm, a_{i4}^\pm]^\top \quad (8)$$

be the sorted vector of partial-wave amplitudes for the i th layer, where “+” and “–” refer to the amplitudes at the upper and lower interfaces of the layer, respectively (Figure 2a). The boundary conditions on the electric and magnetic fields (continuous parallel components across an interface) can be written as (Yeh, 1980; see Supporting Information S1 for details):

$$\mathbf{a}_i^- = \mathbf{L}_i \mathbf{a}_{i+1}^+, \quad (9)$$

which relates the amplitudes on either side of the interface between layers i and $i + 1$ by the interface matrix \mathbf{L}_i (Figure 2a) that depends on the eigenpolarizations.

Finally, a phase change is accumulated as the partial waves propagate through the i th layer. The propagation matrix \mathbf{P}_i describes the change in complex amplitudes between the lower (–) and upper (+) interface of layer i (Figure 2a), such that (Yeh, 1980; see Supporting Information S1 for details):

$$\mathbf{a}_i^+ = \mathbf{P}_i \mathbf{a}_i^- \quad (10)$$

3.3. Radar Returns

Let the surface layer (incident medium, i.e., air) be isotropic ($\langle \mathbf{c} \otimes \mathbf{c} \rangle_0 = \mathbf{I}/3$) such that wave amplitudes can be separated into p and s modes, and let $\mathbf{w} = [w_p, w_s]^T$ be the downward-transmitted p and s complex wave amplitudes at the interface of the surface layer ($i = 0$). We then denote the received wave amplitude resulting from a reflection on the interface between layers i and $i + 1$ by $\mathbf{u}_i = [u_{ip}, u_{is}]^T$.

In the Supporting Information S1, we show how the reflection and transmission coefficients may be determined for each interface given \mathbf{L}_i , and how the corresponding 2×2 reflection and transmission matrices may be constructed. Similar to the radar model by Fujita et al. (2006), transmitted waves that propagate downwards, are reflected of the interface between layers i and $i + 1$, and propagate back up, have received amplitudes given by the matrix product:

$$\mathbf{u}_i = \mathbf{U}_i \mathbf{R}_i \mathbf{D}_i \mathbf{w}. \quad (11)$$

The 2×2 matrices \mathbf{D}_i and \mathbf{U}_i represent the net effect of transmission and propagation down to and up from the reflecting interface, respectively, and \mathbf{R}_i accounts for the reflection (see Supporting Information S1).

Notice that with the spectral representation of ψ , rotating the model antennae system through an angle of β in the horizontal plane (around the vertical axis, $\hat{\mathbf{z}}$) corresponds to shifting the phases of $\hat{\psi}_i^m$ in each layer according to the linear transformation $\hat{\psi}_i^m \rightarrow e^{im\beta} \hat{\psi}_i^m$. In our coordinate system characterized by α and β , the p and s directions thus align with the coordinate axes $\hat{\mathbf{x}}''$ and $\hat{\mathbf{y}}''$, respectively, defined in Figure 2b.

4. Numerical Experiments

To quantify how fabrics without a vertical principal direction (i.e., $\hat{\psi}_2^1 \neq 0$) affect radar returns, we construct a 2 km tall synthetic fabric profile designed to make the effect as clear as possible. Specifically, we consider an ODF profile consisting of a single maximum that is vertical ($\theta = 0$) near the surface and is linearly rotated with depth toward the horizontal plane ($\theta = 90^\circ$). In layer $i = 1$, we therefore set $\hat{\psi}_2^0 = 0.3$ (all other components vanish) and rotate the resulting structure tensor, $\langle \mathbf{c} \otimes \mathbf{c} \rangle_1$, with depth. We furthermore let the single maximum strengthen with depth to make the effect more clear by producing nontrivial radar returns (nonvanishing nodal structure in the angular power anomaly plots below). Note that our conclusions are unchanged by how much the fabric strengthens with depth. The resulting ODFs and eigenvalues of $\langle \mathbf{c} \otimes \mathbf{c} \rangle$ (denoted λ_n) with depth are shown in Figures 3a–3d, respectively.

We mention in passing that we also considered other fabric profiles, but refer the reader to the discussion and Supporting Information S1 for details.

4.1. Radar Model Configuration

The model parameters are chosen to closely follow Fujita et al. (2006). Transmitted waves therefore have a frequency of 179 MHz and are normally incident ($\alpha = 0^\circ$) on the surface interface. The real-valued permittivities are set to $\epsilon'_\perp = 3.17$ and $\epsilon'_\parallel = 3.136$ (i.e., $\epsilon'_\perp - \epsilon'_\parallel = 0.034$), representing isothermal ice at $\sim -25^\circ\text{C}$. The imaginary part of the bulk permittivity is assumed to be dominated by the impurity content content of polar ice, rather than the (pure) single-crystal contributions ϵ''_\perp and ϵ''_\parallel in Equation 2. The imaginary part is therefore isotropic and given by $\text{Im}[\langle \epsilon_g \rangle] = -\sigma/(\omega\epsilon_0)\mathbf{I}$, where the conductivity is taken to be $\sigma = 1 \times 10^{-5} \text{ S m}^{-1}$ (Fujita et al., 2006). Upon setting $\epsilon''_\perp = \epsilon''_\parallel = \sigma/(\omega\epsilon_0)$ our model (Equation 2) reproduces $\text{Im}[\langle \epsilon_g \rangle] = -\sigma/(\omega\epsilon_0)\mathbf{I}$.

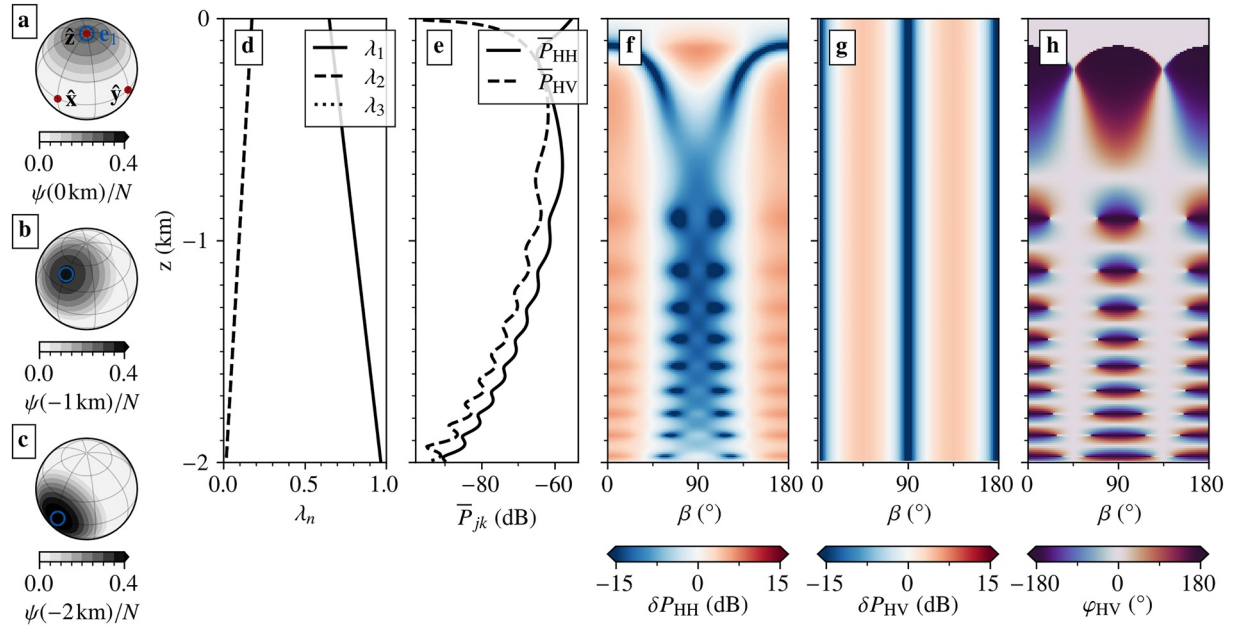


Figure 3. Radar returns given the synthetic orientation distribution function (ODF) profile. (a–c): ODF at selected depths and largest-eigenvalue principal direction \mathbf{e}_1 (blue circle). (d): Eigenvalue profiles (λ_2 and λ_3 overlap). (e): Mean return power. (f and g): HH and HV angular power anomalies. (h): HH–VV coherence phase angle.

4.2. Return Power Metrics

We characterize the modeled radar returns using the usual return-power metrics for phase-sensitive radars. Let therefore the transmitted plane wave be either H- or V-polarized: $\mathbf{w}_H = [w_p, 0]^T$ or $\mathbf{w}_V = [0, w_s]^T$, respectively, for a given β . We furthermore separate the received wave amplitudes into their H- and V-polarized components: $u_H(z, \mathbf{w}) = u_p(z, \mathbf{w})$ and $u_V(z, \mathbf{w}) = u_s(z, \mathbf{w})$, respectively, for a given β , where the depth dependency is for clarity written in terms of z instead of the layer index i . The received angular power anomalies are then:

$$\delta P_{jk}(z) = 20 \log_{10} \|u_k(z, \mathbf{w}_j)\| - \bar{P}_{jk}(z), \quad (12)$$

for transmitted polarizations of $j = H, V$ and received polarizations of $k = H, V$. The mean power is simply the average over β : $\bar{P}_{jk}(z) = 20/\pi \log_{10} \int_0^\pi \|u_k(z, \mathbf{w}_j)\| d\beta$. To quantify the phase difference between the two received polarizations, we adopt the coherence phase (Dall, 2010):

$$\varphi_{jk}(z) = \arg \left(\frac{u_j(z, \mathbf{w}_j) u_k^*(z, \mathbf{w}_k)}{\|u_j(z, \mathbf{w}_j)\| \|u_k^*(z, \mathbf{w}_k)\|} \right), \quad (13)$$

where φ_{HV} is the usual HH–VV coherence phase angle.

5. Results

Figures 3e–3h show the modeled returns \bar{P}_{jk} , δP_{HH} , δP_{HV} , and φ_{HV} , respectively. Note that surface reflections are not shown, and that only the mean power, \bar{P}_{jk} , but not the power anomaly, δP_{jk} , scales with the magnitude of the conductivity, σ . In line with existing transfer matrix models (and measured returns) for fabric profiles that strengthen with depth (e.g., Young, Martín, et al., 2021), a reduction in the vertical spacing between nodes in δP_{HH} and φ_{HV} is found, and δP_{HV} displays a depth-constant 90° periodicity (although the depth-constant pattern may break if the horizontal projection of the principal fabric directions are misaligned between adjacent layers). We refer the reader to, for example, Brisbourne et al. (2019) and Young, Martín, et al. (2021) for further details on the interpretation of polarimetric radar return profiles.

In Figure 4d, the difference is shown between δP_{HH} as modeled given the true ODF profile (Figures 3a–3c) and upon setting $\psi_2^1 = 0$ in the true profile (Figures 4a–4c), henceforth referred to as $\psi^*(z)$. The returns are found to be relatively insensitive to ψ_2^1 (note the colorbar scale in Figure 4d compared to Figure 3f), with the 95th and 99th

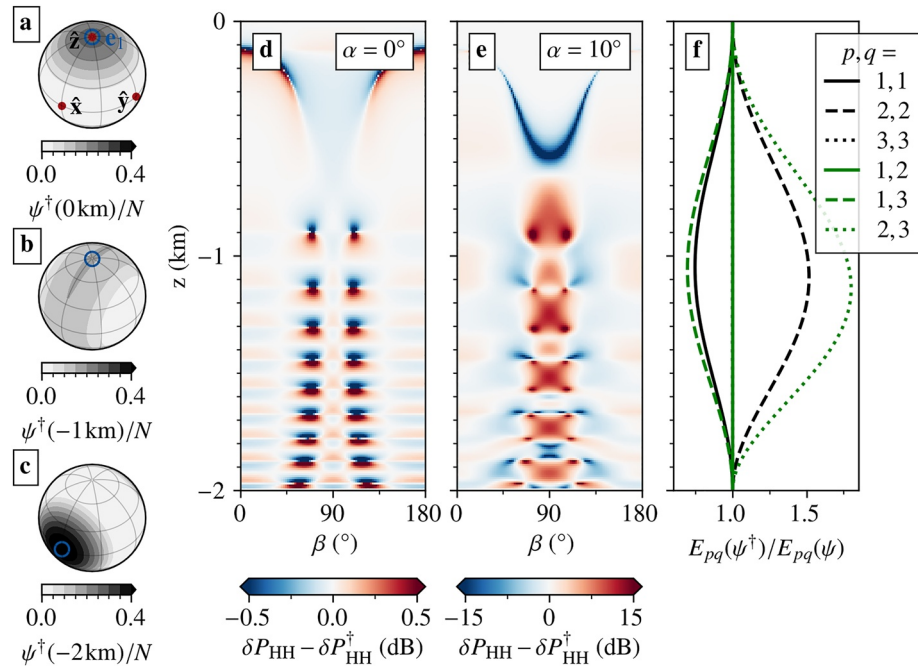


Figure 4. (a–c): ψ^\dagger/N at selected depths (i.e., the orientation distribution function [ODF] assuming that $\hat{\psi}_2^1 = 0$). (d): Difference in modeled δP_{HH} between the ODF profiles ψ/N and ψ^\dagger/N for $\alpha = 0^\circ$. (e): Same as (d) but for $\alpha = 10^\circ$. (f): Relative enhancement factor profiles in the principal directions of the true ODF.

percentile of the absolute differences, $|\delta P_{HH} - \delta P_{HH}^\dagger|$, being 0.3 and 1 dB, respectively. Differences in δP_{HV} and φ_{HV} were found to be negligible.

6. Discussion

It is clear from Figure 4d that neglecting the harmonic mode $(l, m) = (2, 1)$ leads to a relatively small error in δP_{HH} , suggesting that radar returns from normally incident waves are effectively insensitive to the magnitude of $\hat{\psi}_2^1$. Thus, existing transfer matrix models that simply neglect $\hat{\psi}_2^1$ (setting the x - z and y - z entries of $(\mathbf{c} \odot \mathbf{c})$ to zero, see Supporting Information S1), such as Fujita's model (Fujita et al., 2006), might in general be accurate. Indeed, we find that Fujita's model with Paren's reflection coefficients (Paren, 1981) produces returns that are virtually identical to our model for a range of synthetic fabric profiles, including profiles without a vertical principal direction such as in Figure 3 (not shown). Note that Fujita's model requires the power reflection coefficients to be specified manually, as opposed to our model where they follow directly from Maxwell's boundary conditions (Equation 9, see Supporting Information S1). While our work therefore supports the continued use of existing transfer matrix models, such as the Fujita-Paren model, the insensitivity to $\hat{\psi}_2^1$ might make it challenging to infer this ODF component from radar data, not least in the presence of noise.

6.1. Oblique Incidence

Interestingly, we find that the error made by neglecting $\hat{\psi}_2^1$ increases substantially for obliquely incident waves. Figure 4e shows that the error in δP_{HH} is much larger for $\alpha = 10^\circ$ (the error becomes even more pronounced for greater α), all else being equal (note the different colorbar scales). Indeed, the corresponding 95th and 99th percentile of the absolute differences, $|\delta P_{HH} - \delta P_{HH}^\dagger|$, are much larger: 9 and 14 dB, respectively. This suggests that $\hat{\psi}_2^1$ could, in principle, be estimated from wide-angle experiments, possibly from a bistatic configuration. The extended capabilities of our model (allowing arbitrary orientation fabrics and oblique incidence) may therefore aid the interpretations of such radar surveys, and possibly be used to build inverse problems analogous to Ershadi et al. (2021). On that note, we emphasize that the transfer matrix model by Matsuoka et al. (2009) provides many of the same extended capabilities as our model does and could therefore equally well be used.

6.2. Robustness of Results

We considered a total of six synthetic fabric profiles to test the effect of neglecting $\hat{\psi}_2^1$. In the Supporting Information S1, the results of the remaining five experiments are shown. These include both vertically and horizontally rotated single maximum and girdle fabrics with depth, an idealized shear-margin-like profile, and an idealized profile for ice flowing over a bedrock bump. The conclusions drawn from all supplementary experiments align with those presented here. However, we emphasize that we are unable to determine whether the insensitivity to $\hat{\psi}_2^1$ is generally valid. Based on the range of our experiments, we nonetheless believe that the insensitivity to $\hat{\psi}_2^1$ might be relatively common. Our work, therefore, stands as an important caveat when attempting to interpret radar surveys.

6.3. Errors in Inferred Directional Viscosities

Given that $\hat{\psi}_2^1$ might be difficult to infer from radar data, it is worth investigating how bulk directional viscosities are affected if $\hat{\psi}_2^1$ is simply neglected. Consider therefore the case where the ODF is weak enough for higher-order harmonic modes to be disregarded ($\hat{\psi}_l^m = 0$ for $l > 2$). In the Supporting Information S1, we show how the resulting directional strain-rate enhancement factors may be calculated, defined as the strain-rate experienced by a material with an anisotropic fabric (subject to a given stress), divided by the strain-rate experienced if the same material were instead isotropic. For our purpose, we consider the enhancement factors along the principal directions of the true ODF ($\mathbf{e}_1, \mathbf{e}_2, \mathbf{e}_3$), typically required by bulk anisotropic flow laws. In this way, let E_{11} denote the compressional/extensional enhancement factor along \mathbf{e}_1 , E_{12} denotes the \mathbf{e}_1 - \mathbf{e}_2 shear enhancement factor, and so on. Figure 4f shows the relative enhancement factor profiles $E_{pq}(\hat{\psi}^\dagger)/E_{pq}(\hat{\psi})$ for the six unique combinations of p and q ($p, q = 1, 2, 3$). Note that for both $\hat{\psi}$ and $\hat{\psi}^\dagger$, one eigenvector is always parallel to $\hat{\mathbf{y}}$, here labeled as \mathbf{e}_3 . Although disregarding higher wave-number ODF modes is a source of uncertainty, Figure 4f suggests that enhancement factors may be over and underestimated by up to 75% and 25%, respectively, if $\hat{\psi}_2^1$ cannot be determined.

More generally, we note that current implementations of normally incident sounding configurations cause large uncertainties in estimated enhancement factors, due to the ability to infer only relative differences between horizontal fabric eigenvalues (Jordan et al., 2020). Wide-angle radar experiments, which enable oblique sounding, can overcome this limitation and recover all eigenvalues independent of each other (Matsuoka et al., 2009). Therefore, adopting such experimental configurations, aided by our model which allows for arbitrary fabrics, offers a potentially novel path toward an empirically based estimation of anisotropic flow parameters.

6.4. Relevance for Elastic Wave Propagation

As noted in the introduction, shear-wave splitting provides an alternative seismic approach for determining the crystal fabric of ice masses and of the mineral aggregate in the upper mantle. The elastic plane-wave equation in momentum space is an eigenvalue problem similar to Equation 5 (Diez & Eisen, 2015; Hellmann et al., 2021; Kerch et al., 2018; see also Supporting Information S1 for details): $\mathbf{Q}\mathbf{u} - \rho\omega^2\mathbf{u} = \mathbf{0}$, where \mathbf{u} is the displacement field of the plane wave, ρ is the mass density, and \mathbf{Q} is the acoustic tensor. At first glance, it would therefore seem that our methodology could be adapted for elastic (seismic) problems, too.

In the simplest case, the bulk elastic constitutive equation may be taken as the monocrystal constitutive equation averaged over all grain orientations, assuming a homogeneous strain field over the polycrystal scale. It follows that \mathbf{Q} depends on both the second- and fourth-order structure tensors (in addition to the monocrystal elastic parameters; see Supporting Information S1), in contrast to the radio-wave problem which depends solely on the second-order structure tensor by virtue of Equation 2. That is, the elastic problem has an increased sensitivity to small-scale structure in $\hat{\psi}$ compared to the electromagnetic problem. To adapt our method, however, further work is needed to construct the corresponding interface matrix, \mathbf{L}_p , which depends on different boundary conditions: all displacement field components must be continuous, as well as the stress-tensor components involving the vertical direction (Lautrup, 2011, p. 409). Moreover, the elastic problem consists of solving for six partial waves (three downward- and three upward-traveling waves, hence a 6×6 problem), and, like the electromagnetic problem, the wave-vector solutions might become degenerate for certain fabrics that should be handled carefully. We leave such developments for future work, but note that we expect it to be feasible to adapt our methodology for elastic plane-wave propagation, too.

7. Conclusion

We adapted the 4×4 transfer matrix formalism from the optics community to construct a radiowave transfer matrix model applicable to vertically layered anisotropic glacier ice. By expanding the grain c -axis distribution in terms of a spherical harmonic series, we found that radar returns over glacier ice are, for normal incidence, insensitive to whether or not a vertical principal fabric direction exists. Instead, the harmonic mode responsible for a nonvertical principal fabric direction might be determined from oblique radar sounding, suggesting future radar surveys ought to consider wide-angle experiments if they seek to infer the full second-order structure tensor. Unless the harmonic mode responsible for a nonvertical principal fabric direction can be determined, we found that substantial errors in calculated directional ice viscosities might occur. Likewise, insofar as the orientation fabric can function as a flow proxy, it would be insensitive to some flow histories. Finally, we discussed the possibility of adapting our method for elastic (seismic) problems. We showed that for a simple strain-homogenization scheme, the problem of elastic plane-wave propagation is similar to that of electromagnetic plane-wave propagation, suggesting that our method might be adapted to also study shear-wave splitting caused by fabric anisotropy.

Data Availability Statement

The transfer matrix model is available at <https://doi.org/10.5281/zenodo.5769549> and includes a Jupyter notebook demo for calculating radar returns for synthetic fabric profiles.

Acknowledgments

The authors sincerely thank editor Mathieu Morlighem, reviewer Reinhard Drews, and an anonymous reviewer for providing comments that greatly improved this article. Most notably, this includes changing the structure of the article, investigating the relevance of our work for elastic wave modeling, and considering a wider range of numerical experiments. The authors also wish to thank Nikolai Passler and Mathieu Jeannin for providing their computer code for calculating L_r . The research leading to these results has received funding from the Villum Investigator grant no. 16572 as part of the IceFlow project.

References

- Bai, Q., Mackwell, S. J., & Kohlstedt, D. L. (1991). High-temperature creep of olivine single crystals I. Mechanical results for buffered samples. *Journal of Geophysical Research: Solid Earth*, 96(B2), 2441–2463. <https://doi.org/10.1029/90JB01723>
- Bouchez, J., & Duval, P. (1982). The fabric of polycrystalline ice deformed in simple shear: Experiments in torsion, natural deformation, and geometrical interpretation. *Texture, Stress, and Microstructure*, 5(3), 171–190. <https://doi.org/10.1155/TSM.5.171>
- Brisbourne, A. M., Martín, C., Smith, A. M., Baird, A. F., Kendall, J. M., & Kingslake, J. (2019). Constraining recent ice flow history at Korff ice rise, West Antarctica, using radar and seismic measurements of ice fabric. *Journal of Geophysical Research: Earth Surface*, 124(1), 175–194. <https://doi.org/10.1029/2018JF004776>
- Dall, J. (2010). Ice sheet anisotropy measured with polarimetric ice sounding radar. In *2010 IEEE international geoscience and remote sensing symposium* (pp. 2507–2510). <https://doi.org/10.1109/IGARSS.2010.5653528>
- Dall, J. (2020). Estimation of crystal orientation fabric from airborne polarimetric ice sounding radar data. In *IGARSS 2020—2020 IEEE international geoscience and remote sensing symposium* (pp. 2975–2978). <https://doi.org/10.1109/IGARSS39084.2020.9323437>
- Diez, A., & Eisen, O. (2015). Seismic wave propagation in anisotropic ice—Part I: Elasticity tensor and derived quantities from ice-core properties. *The Cryosphere*, 9(1), 367–384. <https://doi.org/10.5194/tc-9-367-2015>
- Duval, P., Ashby, M. F., & Anderman, I. (1983). Rate-controlling processes in the creep of polycrystalline ice. *The Journal of Physical Chemistry*, 87(21), 4066–4074. <https://doi.org/10.1021/j100244a014>
- Ershadi, M. R., Drews, R., Martín, C., Eisen, O., Ritz, C., Corr, H., et al. (2021). Polarimetric radar reveals the spatial distribution of ice fabric at domes in East Antarctica. *The Cryosphere Discussions*, 2021, 1–34. <https://doi.org/10.5194/tc-2020-370>
- Fouch, M. J., & Rondey, S. (2006). Seismic anisotropy beneath stable continental interiors. *Physics of the Earth and Planetary Interiors*, 158(2), 292–320. <https://doi.org/10.1016/j.pepi.2006.03.024>
- Fujita, S., Maeno, H., & Matsuoka, K. (2006). Radio-wave depolarization and scattering within ice sheets: A matrix-based model to link radar and ice-core measurements and its application. *Journal of Glaciology*, 52(178), 407–424. <https://doi.org/10.3189/172756506781828548>
- Fujita, S., Matsuoka, T., Ishida, T., Matsuoka, K., & Mae, S. (2000). A summary of the complex dielectric permittivity of ice in the megahertz range and its applications for radar sounding of polar ice sheets. In T. Hondoh (Ed.), *Physics of ice core records* (pp. 185–212).
- Gammon, P. H., Kieffe, H., Clouter, M. J., & Denner, W. W. (1983). Elastic constants of artificial and natural ice samples by Brillouin spectroscopy. *Journal of Glaciology*, 29(103), 433–460. <https://doi.org/10.3189/S0022143000030355>
- Gillet-Chaulet, F., Gagliardini, O., Meyssonier, J., Montagnat, M., & Castelnau, O. (2005). A user-friendly anisotropic flow law for ice sheet modeling. *Journal of Glaciology*, 51(172), 3–14. <https://doi.org/10.3189/172756505781829584>
- Hargreaves, N. D. (1978). The radio-frequency birefringence of polar ice. *Journal of Glaciology*, 21(85), 301–313. <https://doi.org/10.3189/S0022143000033499>
- Hellmann, S., Grab, M., Kerch, J., Löwe, H., Bauder, A., Weikusat, I., & Maurer, H. (2021). Acoustic velocity measurements for detecting the crystal orientation fabrics of a temperate ice core. *The Cryosphere*, 15(7), 3507–3521. <https://doi.org/10.5194/tc-15-3507-2021>
- Jackson, M., & Kamb, B. (1997). The marginal shear stress of Ice Stream B, West Antarctica. *Journal of Glaciology*, 43(145), 415–426. <https://doi.org/10.3189/S0022143000035000>
- Jordan, T. M., Schroeder, D. M., Elsworth, C. W., & Siegfried, M. R. (2020). Estimation of ice fabric within Whillans Ice Stream using polarimetric phase-sensitive radar sounding. *Annals of Glaciology*, 61(81), 74–83. <https://doi.org/10.1017/aog.2020.6>
- Kerch, J., Diez, A., Weikusat, I., & Eisen, O. (2018). Deriving micro- to macro-scale seismic velocities from ice-core c axis orientations. *The Cryosphere*, 12(5), 1715–1734. <https://doi.org/10.5194/tc-12-1715-2018>
- Kumazawa, M., & Anderson, O. L. (1969). Elastic moduli, pressure derivatives, and temperature derivatives of single-crystal olivine and single-crystal forsterite. *Journal of Geophysical Research*, 74(25), 5961–5972. <https://doi.org/10.1029/JB074i025p05961>
- Lautrup, B. (2011). *Physics of continuous matter: Exotic and everyday phenomena in the macroscopic world*. CRC press. <https://doi.org/10.1201/9781439894200>
- Lilien, D. A., Rathmann, N. M., Hvidberg, C. S., & Dahl-Jensen, D. (2021). Modeling ice-crystal fabric as a proxy for ice-stream stability. *Journal of Geophysical Research: Earth Surface*, 126(9), e2021JF006306. <https://doi.org/10.1029/2021JF006306>

- Llorens, M. G., Griera, A., Bons, P. D., Weikusat, I., Prior, D., Gomez-Rivas, E., et al. (2021). Can changes in ice sheet flow be inferred from crystallographic preferred orientations? *The Cryosphere Discussions*, 2021, 1–24. <https://doi.org/10.5194/tc-2021-224>
- Long, M. D., & Becker, T. W. (2010). Mantle dynamics and seismic anisotropy. *Earth and Planetary Science Letters*, 297(3), 341–354. <https://doi.org/10.1016/j.epsl.2010.06.036>
- Martin, C., Gudmundsson, G. H., Pritchard, H. D., & Gagliardini, O. (2009). On the effects of anisotropic rheology on ice flow, internal structure, and the age-depth relationship at ice divides. *Journal of Geophysical Research: Earth Surface*, 114(F4). <https://doi.org/10.1029/2008JF001204>
- Matsuoka, K., Wilen, L., Hurley, S. P., & Raymond, C. F. (2009). Effects of birefringence within ice sheets on obliquely propagating radio waves. *IEEE Transactions on Geoscience and Remote Sensing*, 47(5), 1429–1443. <https://doi.org/10.1109/TGRS.2008.2005201>
- Monz, M. E., Huddlestone, P. J., Prior, D. J., Michels, Z., Fan, S., Negrini, M., et al. (2021). Full crystallographic orientation (*c* and *a* axes) of warm, coarse-grained ice in a shear-dominated setting: A case study, Storglaciären, Sweden. *The Cryosphere*, 15(1), 303–324. <https://doi.org/10.5194/tc-15-303-2021>
- Paren, J. G. (1981). Reflection coefficient at a dielectric interface. *Journal of Glaciology*, 27(95), 203–204. <https://doi.org/10.3189/S0022143000011400>
- Passler, N. C., Jeannin, M., & Paarmann, A. (2020). Layer-resolved absorption of light in arbitrarily anisotropic heterostructures. *Physical Review B: Condensed Matter*, 101, 165425. <https://doi.org/10.1103/PhysRevB.101.165425>
- Passler, N. C., & Paarmann, A. (2017). Generalized 4×4 matrix formalism for light propagation in anisotropic stratified media: Study of surface phonon polaritons in polar dielectric heterostructures. *Journal of the Optical Society of America B*, 34(10), 2128–2139. <https://doi.org/10.1364/JOSAB.34.002128>
- Qi, C., Prior, D. J., Craw, L., Fan, S., Llorens, M.-G., Griera, A., et al. (2019). Crystallographic preferred orientations of ice deformed in direct-shear experiments at low temperatures. *The Cryosphere*, 13(1), 351–371. <https://doi.org/10.5194/tc-13-351-2019>
- Rathmann, N. M., Hvidberg, C. S., Grinsted, A., Lilien, D. A., & Dahl-Jensen, D. (2021). Effect of an orientation-dependent nonlinear grain fluidity on bulk directional enhancement factors. *Journal of Glaciology*, 67, 1–575. <https://doi.org/10.1017/jog.2020.117>
- Thorsteinsson, T., Waddington, E. D., & Fletcher, R. C. (2003). Spatial and temporal scales of anisotropic effects in ice sheet flow. *Annals of Glaciology*, 37, 40–48. <https://doi.org/10.3189/172756403781815429>
- Wang, B., Tian, G., Sun, B., & Cui, X.-B. (2009). The study of the COF feature in the Antarctic ice sheet based on 3-D anisotropy FDTD method. *Chinese Journal of Geophysics*, 52(2), 413–423. <https://doi.org/10.1002/cjg2.1361>
- Wang, B., & Wong, H. (2020). Analytic solutions to reflection-transmission problem of interface in anisotropic ice sheet. *International Journal of Antennas and Propagation*, 2020, 1, 17. <https://doi.org/10.1155/2020/9869873>
- Wang, W., & Becker, T. W. (2019). Upper mantle seismic anisotropy as a constraint for mantle flow and continental dynamics of the North American plate. *Earth and Planetary Science Letters*, 514, 143–155. <https://doi.org/10.1016/j.epsl.2019.03.019>
- Warren, C., Giannopoulos, A., & Giannakis, I. (2016). gprMAX: Open source software to simulate electromagnetic wave propagation for ground penetrating radar. *Computer Physics Communications*, 209, 163–170. <https://doi.org/10.1016/j.cpc.2016.08.020>
- Wilson, C. J., & Peterzell, M. (2011). Evaluating ice fabrics using fabric analyzer techniques in Sørskal Glacier, East Antarctica. *Journal of Glaciology*, 57(205), 881–894. <https://doi.org/10.3189/002214311798043744>
- Xu, W., Wood, L. T., & Golding, T. D. (2000). Optical degeneracies in anisotropic layered media: Treatment of singularities in a 4×4 matrix formalism. *Physical Review B: Condensed Matter*, 61, 1740–1743. <https://doi.org/10.1103/PhysRevB.61.1740>
- Yeh, P. (1980). Optics of anisotropic layered media: A new 4×4 matrix algebra. *Surface Science*, 96(1), 41–53. [https://doi.org/10.1016/0039-6028\(80\)90293-9](https://doi.org/10.1016/0039-6028(80)90293-9)
- Young, T. J., Martín, C., Christoffersen, P., Schroeder, D., Tulaczyk, S., & Dawson, E. (2021). Rapid and accurate polarimetric radar measurements of ice crystal fabric orientation at the Western Antarctic Ice Sheet (WAIS) Divide deep ice core site. *The Cryosphere*, 15(8), 4117–4133. <https://doi.org/10.5194/tc-15-4117-2021>
- Young, T. J., Schroeder, D. M., Jordan, T. M., Christoffersen, P., Tulaczyk, S. M., Culberg, R., & Bienert, N. L. (2021). Inferring ice fabric from birefringence loss in airborne radargrams: Application to the eastern shear margin of Thwaites Glacier, West Antarctica. *Journal of Geophysical Research: Earth Surface*, 126(5), e2020JF006023. <https://doi.org/10.1029/2020JF006023>

References From the Supporting Information

- Garibello, B., Avilán, N., Galvis, J. A., & Herreño-Fierro, C. A. (2020). On the singularity of the yeh 4×4 transfer matrix formalism. *Journal of Modern Optics*, 67(9), 832–836. <https://doi.org/10.1080/09500340.2020.1775905>
- Jeannin, M. (2020). Layer-resolved absorption of light in arbitrarily anisotropic heterostructures (Python files). *Zenodo*. <https://doi.org/10.5281/zenodo.3724504>
- Maurel, A., Lund, F., & Montagnat, M. (2015). Propagation of elastic waves through textured polycrystals: Application to ice. *Proceedings of the Royal Society A: Mathematical, Physical and Engineering Sciences*, 471(2177), 20140988. <https://doi.org/10.1098/rspa.2014.0988>
- Passler, N. C., & Paarmann, A. (2019). Generalized 4×4 matrix formalism for light propagation in anisotropic stratified media: Study of surface phonon polaritons in polar dielectric heterostructures: Erratum. *Journal of the Optical Society of America B*, 36(11), 3246–3248. <https://doi.org/10.1364/JOSAB.36.003246>
- Rathmann, N. M., & Lilien, D. A. (2021). Inferred basal friction and mass flux affected by crystal-orientation fabrics. *Journal of Glaciology*, 1–17. <https://doi.org/10.1017/jog.2021.88>
- Weiyi, C. (1999). Derivation of the general form of elasticity tensor of the transverse isotropic material by tensor derivate. *Applied Mathematics and Mechanics*, 20(3), 309–314. <https://doi.org/10.1007/BF02463857>